

# Charge Transport and Space-Charge Formation in $\text{Cd}_{1-x}\text{Zn}_x\text{Te}_{1-y}\text{Se}_y$ Radiation Detectors

J. Pipek<sup>1,\*</sup>, M. Betušiak<sup>1</sup>, E. Belas<sup>1</sup>, R. Grill<sup>1</sup>, P. Praus<sup>1</sup>, A. Musiienko<sup>1</sup>, J. Pekarek<sup>1</sup>, U.N. Roy<sup>2,3</sup>, and R.B. James<sup>3</sup>

<sup>1</sup>Charles University, Faculty of Mathematics and Physics, Institute of Physics, Ke Karlovu 5, CZ-121 16, Prague 2, Czech Republic

<sup>2</sup>Brookhaven National Laboratory, Upton, New York 11973, USA

<sup>3</sup>Savannah River National Laboratory, Aiken, South Carolina 29808, USA



(Received 26 January 2021; revised 21 April 2021; accepted 27 April 2021; published 26 May 2021)

The electron- and hole-transport properties in cadmium zinc telluride (CZTS) crystals are studied using a laser-induced transient-current technique with pulsed and dc bias. The internal electric field profile and velocity of surface recombination are determined by Monte Carlo simulations of electron and hole transient currents combined with a numerical solution of the drift-diffusion equation coupled with Poisson's equation. Electron and hole drift mobilities of  $\mu_e = 830 \text{ cm}^2/\text{Vs}$  and  $\mu_h = 40 \text{ cm}^2/\text{Vs}$ , respectively, are determined. We also develop a simple technique for evaluating surface recombination directly from measured current waveforms without the need for numerical simulation. The good quality of the prepared detector at pulsed bias, with electron- and hole-mobility-lifetime products of  $(\mu\tau)_e = 1.9 \times 10^{-3} \text{ cm}^2/\text{V}$  and  $(\mu\tau)_h = 1.4 \times 10^{-4} \text{ cm}^2/\text{V}$ , respectively, are observed. The formation of a positive space charge, originating from hole injection combined with a recombination level, is found. We observe a significant position dependence of the lifetime of electrons and holes in dc bias due to hole injection. The experiment is successfully fitted by a simple model dominated by a single deep recombination level with an energy of  $E_i = E_C - 0.73 \text{ eV}$ ; concentration of  $7.3 \times 10^{11} \text{ cm}^{-3}$ ; and electron- and hole-capture cross sections of  $3.5 \times 10^{-14} \text{ cm}^2$  and  $6.5 \times 10^{-14} \text{ cm}^2$ , respectively.

DOI: 10.1103/PhysRevApplied.15.054058

## I. INTRODUCTION

Semiconductor radiation detectors are nowadays widely used for the convenience of the direct conversion of x-rays and gamma rays into electrical signals. The spatial localization of generated electric charge within the detector's bulk enhances their resolution compared with other detectors, namely, scintillators. Semiconducting detectors are important for applications in advanced medical imaging systems using lower radiation doses and providing a higher spatial resolution of biological tissue. Today, cadmium zinc telluride (CZT) is the most advanced room-temperature semiconducting material for such detection [1]. While basic binary CdTe assures high radiation absorption and sufficient band-gap energy, Zn is added to the material to increase the band gap and the resistivity. Despite recent progress in CZT technology [2], it suffers from several inconvenient problems: nonunity segregation coefficient of Zn in the range 1.05 to 1.6, depending on the growth method and Zn content [3]; abundant emergence of crystal defects and networks (such as subgrain

boundaries); and high concentrations of Te inclusions or precipitates [4,5]. These issues result in a low yield and high cost of high-quality CZT radiation detectors, which limit their applications. Researchers have tried to solve these issues by improving the crystal-growth process and by postgrowth annealing, but they have not yet mitigated all of these disadvantages [6,7].

Selenium is found to be a very effective element in reducing the complications mentioned above [8,9]. In addition, the Se segregation coefficient is near unity in the CdTe matrix. The quaternary semiconductor  $\text{Cd}_{1-x}\text{Zn}_x\text{Te}_{1-y}\text{Se}_y$  (CZTS) is expected to resolve long-standing problems associated with CZT material. The role of selenium in this semiconductor is [9,10] (a) a strong influence on the Zn segregation coefficient, and thus, better compositional homogeneity; (b) effective solution hardening in arresting subgrain boundaries and their networks; and (c) decreased Te inclusion or precipitate concentration. Hence, high-performance detector-grade CZTS material can be potentially produced at a lower cost [11].

Here, we investigate charge transport in the CZTS detector under pulsed and dc bias using a laser-induced transient-current technique. We observe a positive space

\*jindrich.pipek@gmail.com

charge that can be eliminated using pulsed bias. Charge-transport parameters are obtained by Monte Carlo (MC) simulations of electron and hole transient currents.

## II. EXPERIMENT

Here, a semi-insulating *p*-type CZTS sample with resistivity of  $1.1 \times 10^{10} \Omega \text{ cm}$ ; dimensions of  $6.9 \times 5 \times 1.7 \text{ mm}^3$ ; and selenium and zinc concentrations of 4% and 10%, respectively, is studied by the laser-induced transient-current technique (LTCT) [12]. The CZTS single crystal is grown by using the traveling heater method at Brookhaven National Laboratory. The source CZT and CdSe materials of 99.9999% purity are used for CZTS synthesis and growth. The band-gap energy at room temperature is  $E_g \approx 1.52 \text{ eV}$  [13]. Two planar electrical contacts are prepared by electroless deposition of gold from a 1% gold chloride methanol-based solution [14]. It has been previously shown that gold forms a quasiohmic contact on CZT material [15], and it is successfully applied for CZTS detectors as well [16,17].

The sample is characterized using LTCT in combination with a pulsed bias, which allows us to suppress the space-charge formation and to study charge-trapping effects on the current waveforms, thus enabling easier evaluation of the electron- (hole-) drift-mobility carrier-trapping and -detraping times [18,19]. Electron (hole) current waveforms are measured by illuminating a semi-transparent cathode (anode) using a laser pulse with an above-band-gap wavelength at 660 nm, which is absorbed in less than  $1 \mu\text{m}$  under the illuminated electrode [20]. Illuminating the cathode (anode), the photogenerated holes (electrons) are immediately collected on the exposed electrode, while carriers with the opposite charge drift toward the other electrode and induce a transient current described by the Shockley-Ramo theorem [21]. The signal is amplified and recorded by a digital sampling oscilloscope (see details in Ref. [12]). A neutral density filter is used to assure that the photogenerated charge is small enough not to affect the electric field inside the detector. Typically, a transient charge of hundreds of fC is used. The laser and bias pulse positions are synchronized as shown in Fig. 1 and characterized by a laser-pulse delay (LPD), bias pulse width (BPW), depolarization time (DT), and pulsing period (PP) [18]. The laser pulse width has a FWHM of about 2 ns. Decreasing the LPD to the microsecond timescale, the space-charge formation induced by carrier injection or depletion induced by nonohmic contacts can be suppressed. This option simplifies the MC simulations, offering the possibility to directly determine the lifetime of drifting carriers from the slope of the current waveform (CWF) [18,22,23].

For the numerical simulation, we combine two approaches routinely used by researchers to simulate charge-transport phenomena in semiconductors, that is, the

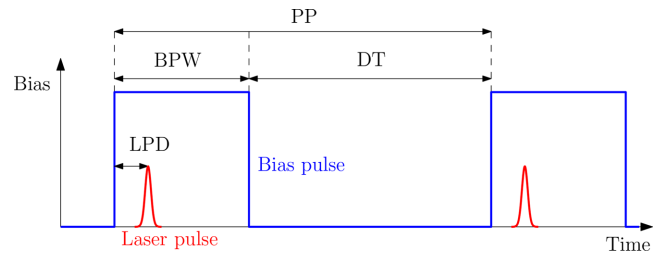


FIG. 1. Scheme of the synchronization of the bias pulse and laser excitation pulse.

solution of the drift-diffusion equation (DDE) coupled with Poisson's equation is combined with the Shockley-Read-Hall model depicting carrier (de)trapping. We develop a custom code [24,25], which allows us to conduct comprehensive simulations of all phenomena occurring in planar samples. Nevertheless, the approach involves an extensive inclusion of spatial derivatives, which are time-consuming when called upon for calculating transient currents. We thus combine our code with the MC method described elsewhere [19]. Here, we embed the electric field profile and recombination-level occupancy calculated at specific conditions as defined by the bias, delay time after biasing, etc. by DDE. MC is then used to calculate the current transient. The combination of both techniques makes the numerical treatment much more efficient and significantly reduces the computation run time.

## III. RESULTS

The bias dependence of the electron and hole CWFs, using a pulsed bias with pulsing parameters  $\text{LPD} = 80 \mu\text{s}$ ,  $\text{BPW} = 200 \text{ ms}$ , and  $\text{DT} = 800 \text{ ms}$ , is shown in Figs. 2(a) and 2(b), respectively. Insets in Fig. 2 show CWF normalized by the respective bias. The LPD is chosen to be short enough to eliminate space-charge formation, and the DT is long enough to suppress the memory effects between consecutive bias pulses. The detector is fully depolarized after each pulse period. No visible changes to the CWF shape are observed with a LPD from 80 to 500  $\mu\text{s}$ . We thus consider the detector to be unpolarized at each bias with a constant electric field for  $\text{LPD} = 80 \mu\text{s}$ . Fast oscillations apparent at the start of the electron waveforms in this and in other figures in this paper are generated by the adjoint electronics. We do not study this feature in detail here. A relevant study may be found in Ref. [18]. The black dashed lines in Figs. 2(a) and 2(b) and in all consecutive figures are the Monte Carlo fits, which are discussed later in sec. IV.

Figure 3(a) shows the bias dependence of the electron CWFs for illumination of the cathode using a dc bias with a laser pulsing period of 1 s. The dashed lines represent the MC simulations. Before measuring CWFs, the detector becomes fully polarized in less than 1 s and retains a stable space charge during measurements. The inset in

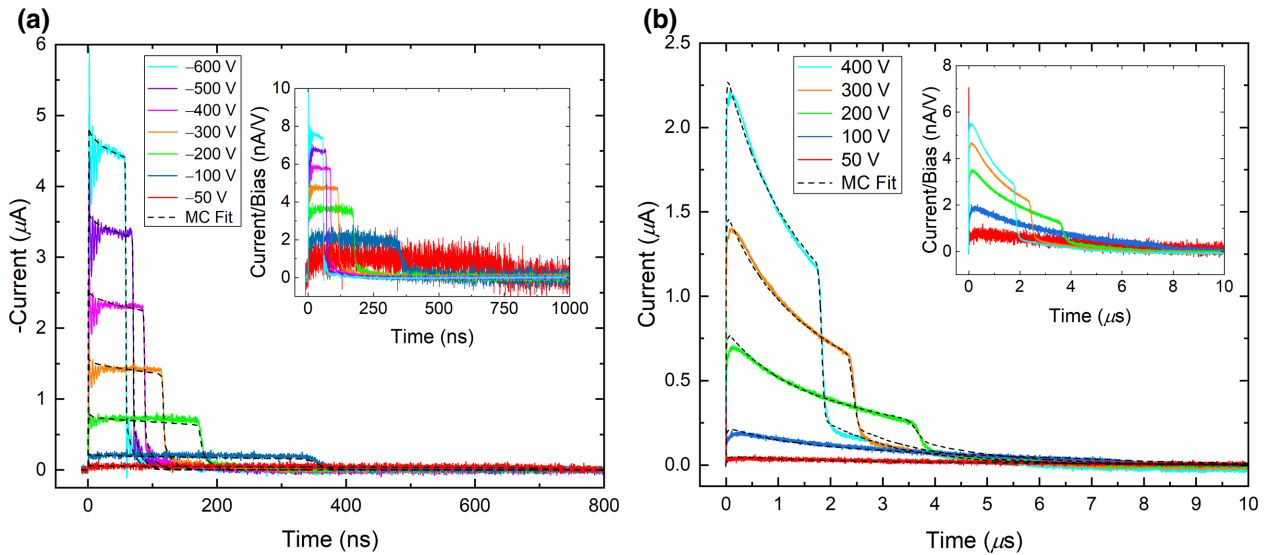


FIG. 2. (a) Pulsed-bias dependence of electron-current waveforms and (b) hole-current waveforms. Dashed lines represent the Monte Carlo fit. Insets show the CWF normalized by respective bias.

Fig. 3(a) shows the bias dependence of the electric field profile within the detector, which reveals a strong electric field dependence on the position inside the detector, with a nearly zero electric field under the anode. Figure 3(b) shows the evolution of the electron CWFs under a  $-400$  V pulsed bias using a LPD ranging from  $80\ \mu\text{s}$  to  $200\ \mu\text{s}$  and PP = 1 s. The corresponding MC simulation is shown by the dashed line. Current waveforms are also measured in the range of laser pulse delays of  $80$ – $500\ \mu\text{s}$ . Since no visible change is observed using a LPD  $< 500\ \mu\text{s}$ , data are not shown in Figs. 3(b) and 3(d). We find that the detector remains fully depolarized in the LPD interval of  $80$ – $500\ \mu\text{s}$  with no apparent space-charge formation, and the CWFs are only slightly damped due to charge trapping. The CZTS material shows long-term stability in the range of pulsed and dc biases used in our experiments. No material change is observed after many hours of applied dc bias, and repeatable results for the LTCT experiments are measured. The main difference between the dc and pulsed biases is the DT, which allows elimination of the space charge. By using a short BPW and long DT, detector polarization can be prevented. Measurements with dc and pulsed biases are otherwise the same. The space-charge formation is caused by the redistribution of charge on the energy levels, and a repeatable result of the LTCT experiment is measured after many hours of applied dc bias. The detector reveals gradual polarization for a LPD  $> 500\ \mu\text{s}$ , which causes the corresponding tilting of the CWF. The polarization saturates around LPD =  $200\ \mu\text{s}$ , when the electric field reaches almost zero value under the illuminated anode. The inset in Fig. 3(b) shows the LPD dependence of the electric field profile obtained by MC simulations, which correlates with space-charge formation.

Analogous experiments illuminating the anode are performed to measure the CWF for holes. Figure 3(c) shows the dc bias dependence of the hole CWF with a laser pulsing period of 1 s, and the inset in Fig. 3(c) shows the electric field obtained from MC simulations. The hole cloud generated under the illuminated anode drifts at the beginning through the area with a relatively low electric field, which amplifies surface recombination due to the low drift velocity [see Eq. (1)]. The low electric field is also responsible for the carrier cloud broadening, which creates the wide tail of the CWF. Figure 3(d) shows the evolution of the hole CWFs under a  $400$  V pulsed bias using a LPD ranging from  $80\ \mu\text{s}$  to  $200\ \mu\text{s}$  and PP = 1 s. The dashed lines represent MC simulations. The inset in Fig. 3(d) shows the evolution of the electric field profile dependence on the LPD, as obtained by MC simulations. We note that the electric field profiles deduced both from the electron and hole LTCT signals are identical within experimental error. This observation verifies our model and affirms the validity of the technique for the characterization of transport properties for both carrier types. The nearly constant depth at which the electric field profiles cross [see inset in Figs. 3(b) and 3(d)] stems from the applied bias ( $-400$  V), which requires a fixed value of the electric field integral over the sample thickness. Since the electric field profile is an almost linear function, the profiles intersect at nearly the same point.

#### IV. MODEL

To describe the electron and hole charge-transport properties in the CZTS sample, the combination of a custom Monte Carlo program based on Ref. [19] with a program solving a one-dimensional coupled Poisson equation

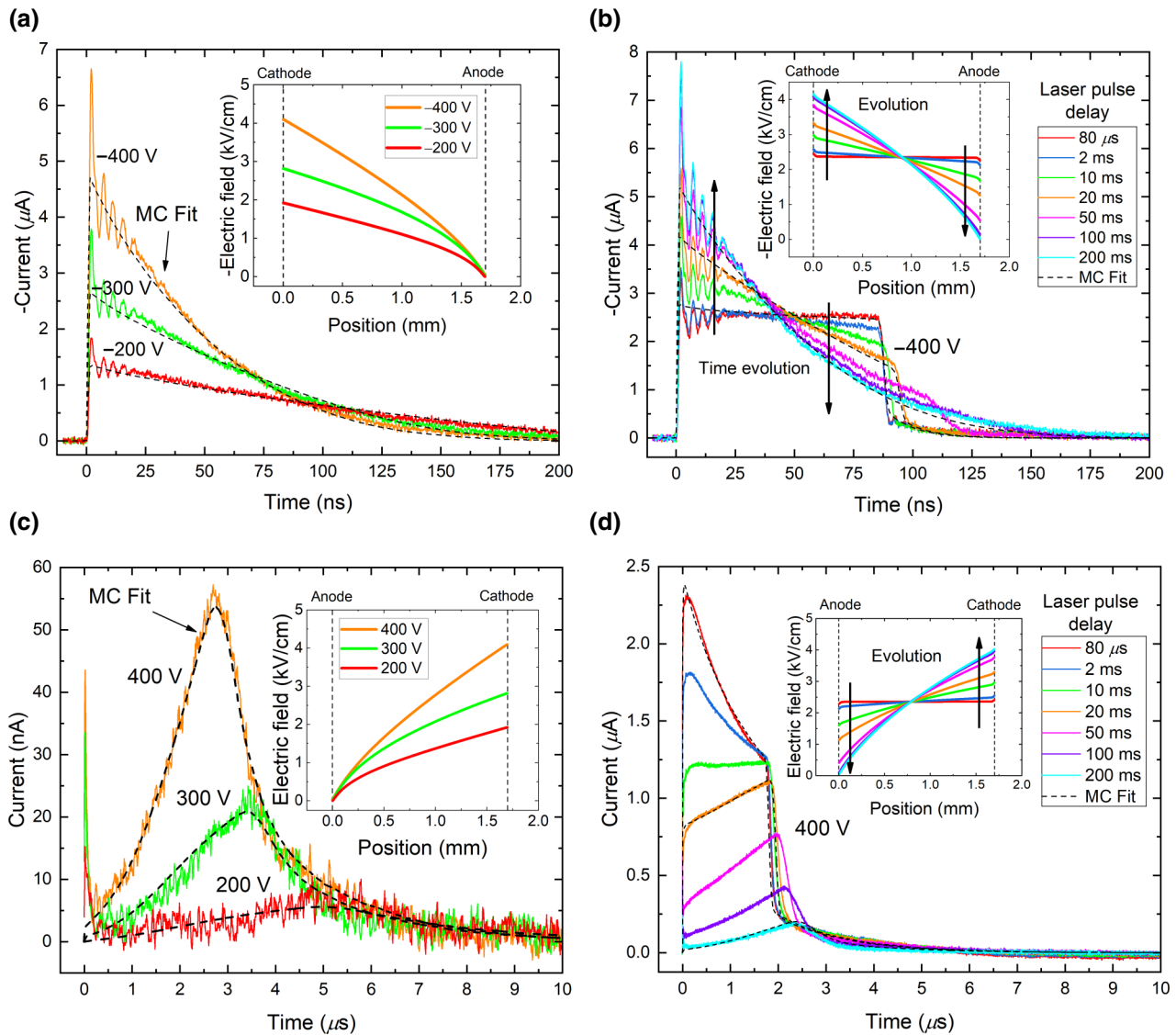


FIG. 3. (a) The dc bias dependence of electron-current waveforms, (b) evolution of electron-current waveforms at a pulsed bias of  $-400\text{ V}$  (arrows show the direction of the electric field evolution) depending on LPD, (c) dc bias dependence of measured hole-current waveforms, and (d) evolution of hole-current waveforms at a pulsed bias of  $400\text{ V}$  depending on LPD. Dashed lines plot the Monte Carlo fit. Insets in (a) and (c) show respective electric field profiles; insets in (b) and (d) represent evolution of the electric field profile within the detector at several different values for the LPD.

and DDE [24,25] is used. The electric field profile and level occupancies are calculated at specific conditions, as defined by the bias, delay time after biasing, etc., by the DDE and inserted into the MC simulation, which is then used to calculate the current waveforms. Three defect levels, which are sufficient to describe all observed effects, are obtained by fits based on the Shockley-Read-Hall model [26]. A schematic of the energy levels is shown in Fig. 4. We evaluate one dominant recombination level with an energy of  $E_t = E_C - 0.73\text{ eV}$ , with a concentration of  $N_t = 7.3 \times 10^{11}\text{ cm}^{-3}$  and electron- and hole-capture cross sections of  $\sigma_e = 3.5 \times 10^{-14}\text{ cm}^2$  and  $\sigma_h = 6.5 \times 10^{-14}\text{ cm}^2$ , respectively. The redistribution of charge

carriers at this deep level is responsible for space-charge formation inside the detector. In addition, one shallow electron trap and one shallow hole trap are added. Carrier trapping and detrapping processes at shallow levels are characterized by the trapping time,  $\tau_T$ , and detrapping time,  $\tau_D$  [19]. The shallow electron trap is characterized by trapping and detrapping times of  $\tau_{eTS} = 300\text{ ns}$  and  $\tau_{eDS} = 10\text{ ns}$ , respectively, and the shallow hole trap is characterized by trapping and detrapping times of  $\tau_{hTS} = 4\text{ }\mu\text{s}$  and  $\tau_{hDS} = 1.2\text{ }\mu\text{s}$ , respectively. Comparable parameters of shallow traps can be found for CdTe and CZT in Ref. [19]. The shallow traps are responsible for charge delay and widening of the CWF fall

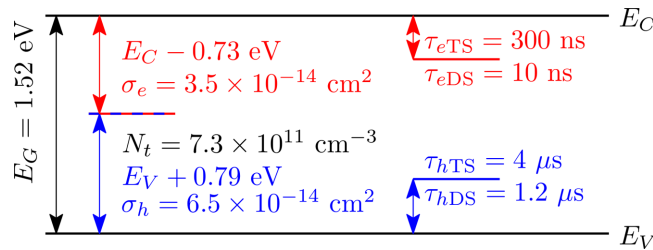


FIG. 4. Schematic of the obtained energy levels with their parameters determined by numerical simulations of LTCT waveforms. Red, electron traps. Blue, hole traps. Red-blue, recombination level.

edge. The energy and concentration of these shallow levels cannot be determined using MC simulations, since there is not enough information conveyed from the LTCT data, and only the trapping and detrapping times can be determined. We use the Fermi-level position in the bulk,  $E_F = E_C - 0.73 \text{ eV}$ , corresponding to the measured sample resistivity of  $1.1 \times 10^{10} \Omega \text{ cm}$ . The contact properties are defined within the drift-diffusion model [24] by the fitted band bending,  $V_B = 90 \text{ meV}$ , evoking electron (hole) depletion (injection). In our case, hole injection is caused by the type of electrical contact. We take advantage of hole injection to determine parameters for the deep recombination level. By using different contact-preparation techniques or contact materials, both hole injection and space charge can be decreased. The search for the ideal contact-preparation technology to optimize the Schottky barrier is beyond the scope of this paper. The Fermi level at the surface is then fixed on both sides at  $E_{F0} = E_C - 0.82 \text{ eV}$ . The electron- and hole-drift mobility obtained from MC simulations is  $\mu_e = 830 \text{ cm}^2/\text{Vs}$  and  $\mu_h = 40 \text{ cm}^2/\text{Vs}$ , respectively, and electron and hole lifetimes connected with the recombination center are  $\tau_e = 2.3 \mu\text{s}$  and  $\tau_h = 3.6 \mu\text{s}$ , respectively. These are similar values of mobilities and lifetimes to those of CZT [19]. The recombination center causes losses of free-drifting charge, leading to decays in the CWF, which are visible in Fig. 2. Thus, the mobility-lifetime products of electrons and holes at pulsed bias are  $(\mu\tau)_e = \mu_e \tau_e = 1.9 \times 10^{-3} \text{ cm}^2/\text{V}$  and  $(\mu\tau)_h = \mu_h \tau_h = 1.4 \times 10^{-4} \text{ cm}^2/\text{V}$ , respectively, which are similar to values in Ref. [11]. The measured electron  $\mu\tau$  product is relatively high and, together with the high  $\mu\tau$  product for holes, the material is ready for the preparation of radiation detectors for different applications. Enhancement of the  $\mu\tau$  product is a technological challenge and depends on the improvement of the crystal quality and reduction of native and extrinsic defects. Lowering the concentration of the recombination level found in this paper is expected to improve the detector quality.

## V. DISCUSSION

The positive space-charge formation in this sample comes from a weak injection of holes from the anode, which creates a positive space charge by trapping at the hole recombination center distributed throughout the whole sample. Subsequently, the positive space charge starts to shield the electric field and dampens hole injection, forming a feedback loop that keeps the electric field almost zero near the anode. Steady state is assured by balancing hole injection, which boosts space-charge formation, and screening of the electric field at the anode, which dampens the process of charging. The principle of electric field screening is independent of the applied bias, so that the space charge is implicitly adjusted to a value sufficient to nearly screen the bias. The model consistently describes all data collected in the range of bias, 50–600 V, used in our experiments. The process of positive space-charge formation stabilizes anode screening at a timescale of 10–100 ms when hole injection is attenuated. This is observed as a saturation in electric field evolution [see the insets of Figs. 3(b) and 3(d)].

The presence of the space charge at dc bias prevents the standard evaluation of the mobility-lifetime product,  $\mu\tau$ , using fitting of the Hecht equation [27]. Likewise, a more advanced procedure [27], incorporating the electric field profile inside the sample, cannot be used, since it builds on charge transport mediated by purely drift current. In the hole-injection regime, the electric field changes sign and is almost zero at the anode under the dc bias due to band bending combined with the positive space charge. Subsequently, integrals defining the charge-collection efficiency in respective formulas diverge. A significant contribution of diffusion current is demonstrated in Fig. 5, where the decomposition of electron and hole currents into drift and diffusion components for a detector under  $-200 \text{ V}$  dc bias is shown. The diffusion current prevails at the anode and decreases into the bulk, where the drift component dominates. We note that both total electron and total hole current densities are not constant in the bulk due to electron-hole recombination through the recombination level.

Monte Carlo simulations can be used for any electric field profile to obtain transport parameters from the LTCT experiments. When combined with the pulsed bias, the mobilities and lifetimes of electrons and holes can be determined separately. The electric field profile can also be obtained, which is not accessible using the Hecht equation. The evaluation of transport parameters in a depolarized sample allows us to obtain material properties without interference from space-charge effects, which complicate the evaluation and affect the lifetime. In the case of a positive space charge, the lifetime of the holes is increased because of the filling of hole-trap states by hole injection. Oppositely, the lifetime of the electrons decreases because of the depletion of electron-trap states. In the case of the

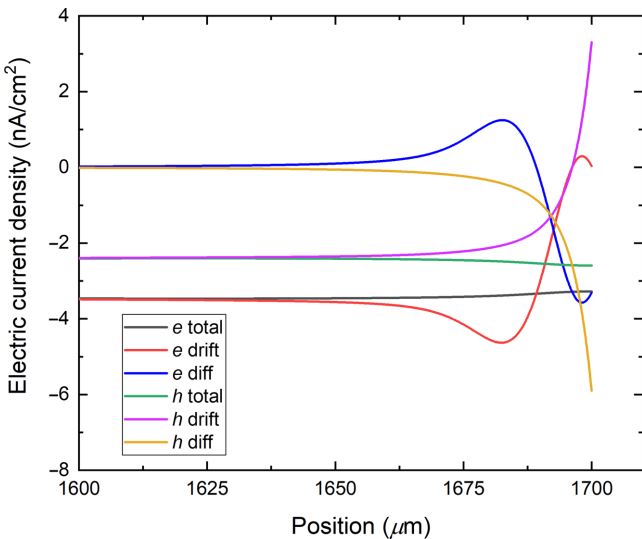


FIG. 5. Decomposition of electron and hole currents into drift and diffusion components for the detector under dc bias at  $-200$  V. Anode is on the right-hand side.

recombination level considered in our model, both features occur in parallel. This phenomenon is demonstrated in Fig. 6, where the profiles of the lifetimes of electrons and holes under pulsed and dc bias  $-400$  V are shown. Under pulsed bias, the lifetime is constant in the bulk and decreases for electrons and increases for holes near the electrodes due to band bending. Under dc bias, a significant redistribution of charge carriers at the recombination level causes a large increase of the lifetime of holes caused by saturation of the recombination level by injected holes, and thus, increases the hole lifetime by an order of magnitude compared with that under pulsed bias. In other words, at the anode, there is a decrease in the lifetime of electrons caused by electron depletion from the recombination level. Since the depletion of electrons is not strong enough to completely negate the effects of the recombination level, the decrease in the electron lifetime is relatively small compared with the increase of the hole lifetime. Lifetime depends on the location in the sample and on the applied bias. In the case of a negative space charge incurred by electron injection from the cathode, the effect would be the opposite.

Significant surface recombination (SR) is found using MC simulations for both electrons and holes. Surface recombination is caused by the presence of surface traps and recombination centers, which are difficult to evaluate through the LTCT technique due to the short time that charge carriers spend in the thin layer under the surface. Here, the corresponding contribution to the current waveform is not visible. Thus, the effective parameter used to describe surface imperfections collectively is the surface recombination velocity,  $s$ , which defines the charge-carrier losses before moving from the surface layer into the

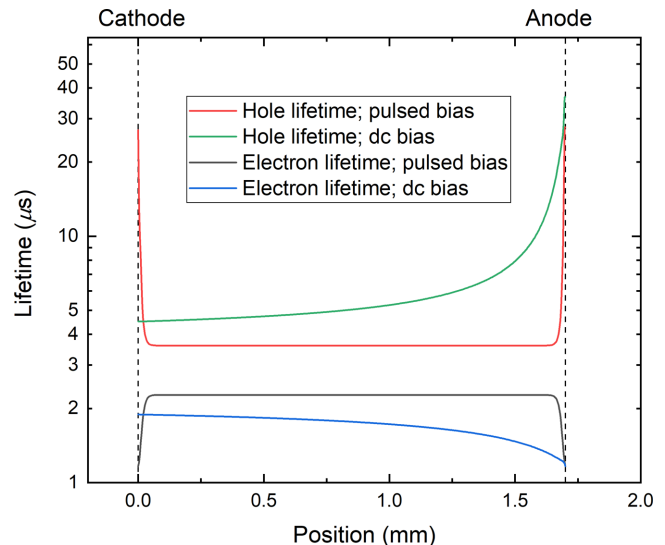


FIG. 6. Profile of lifetimes of electrons and holes under pulsed and dc biases of  $-400$  V.

bulk [19]. In our case, the surface recombination velocity is independent of the laser intensity for all ranges used in this paper. It is, however, dependent on the surface treatment, aging, handling, and other surface-related conditions.

The initially photogenerated charge,  $Q_{00}$ , in the surface layer partially recombines. The remaining charge entering the bulk,  $Q_0$ , is

$$Q_0 = Q_{00} \frac{v}{v + s}, \quad (1)$$

where  $v$  is the charge-carrier drift velocity in the surface layer. In our case of a depolarized detector, the electric field is constant over the whole detector, thus the drift velocity is given by  $v = \mu E_0 = \mu U/L$ , where  $E_0$  is the electric field in the surface layer,  $U$  is the applied bias,  $L$  is the sample thickness, and  $\mu$  is either the electron- or hole-drift mobility depending on the type of drifting carriers. Using constant drift velocity  $v$ , from Eq. (1) we obtain

$$Q_0 = Q_{00} \frac{1}{1 + (sL/\mu U)}. \quad (2)$$

The current waveform for electrons (and respectively for holes) shortly after carrier generation before any significant trapping in the bulk is given according to the Shockley-Ramo theorem [21]:

$$I(t) = \frac{Q_0 v}{L} = \frac{Q_{00} \mu U}{L^2} \frac{\mu U}{sL + \mu U}. \quad (3)$$

As it is apparent from Eq. (3), in the case of negligible surface recombination, where  $s \ll \mu U/L$ , the onset of the CWFs divided by respective bias,  $I(t = 0)/U$ , should start

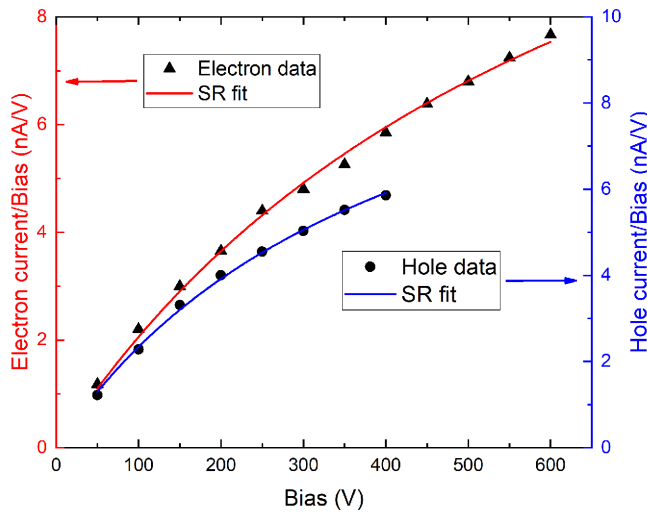


FIG. 7. Bias dependence of initial values of current waveforms of electrons and holes under pulsed bias. Solid lines represent fits using Eq. (3); red, electrons; blue, holes.

from the same bias-independent value. Alternatively, in the case of distinct surface recombination,  $I(t = 0)/U$  depends on the bias. This feature is seen in the insets of Figs. 2(a) and 2(b), where the CWFs of electrons and holes normalized by respective bias are shown. Distinct starts of the normalized CWFs are clearly seen, proving the presence of significant surface recombination at both contacts. Bias dependence of the initial values of electron- and hole-current waveforms divided by the respective bias taken from insets of Fig. 2 are shown in Fig. 7. Fitting using Eq. (3) is shown with a red line for electrons and a blue line for holes. The surface recombination velocity for electrons,  $s_e = 3.3 \times 10^6 \text{ cm/s}$ , and holes,  $s_h = 9.8 \times 10^4 \text{ cm/s}$ , are evaluated. This represents an easy method to calculate surface recombination directly from measured current waveforms without the need for Monte Carlo simulation. This method serves as a simple way to detect the presence of surface recombination in the detector and helps with the MC simulations of the CWF.

It should be noted that positive space-charge formation caused by the injecting anode shows distinct characteristics from the more frequently used model describing positive space-charge formation induced by electron depletion affected by the blocking cathode [22,23]. There appears to be an extensive inactive region, essentially a dead layer, near the anode, which appears due to electric field screening by the excessive positive space charge localized under the cathode. Consequently, the LTCT signal of holes cannot be measured, unlike in our case, where the hole signal is detected. The nature of the defect responsible for charging is different in the case of electron depletion. While the model presented in this paper considers hole trapping, where injected holes are stored, depleted electrons induce

positive space charge by the electron trap detrapping previously deposited electrons. While hole injection and the rate of polarization are ruled by the Schottky barrier at the anode, polarization induced by electron depletion is defined by the electron-trap energy, which is expressed relative to the conduction band.

## VI. CONCLUSION

We measure the electron- and hole-current transients in a CZTS detector using LTCT for pulsed and dc biases. A theoretical model of space-charge formation based on the Shockley-Read-Hall model is developed and successfully applied, assuming positive space-charge formation due to hole injection combined with the existence of the recombination level. We identify one dominant recombination level with an energy of  $E_t = E_C - 0.73 \text{ eV}$ ; concentration of  $7.3 \times 10^{11} \text{ cm}^{-3}$ ; and electron- and hole-capture cross sections of  $3.5 \times 10^{-14} \text{ cm}^2$  and  $6.5 \times 10^{-14} \text{ cm}^2$ , respectively, together with one shallow electron trap characterized by trapping and detrapping times of  $\tau_{eTS} = 300 \text{ ns}$  and  $\tau_{eDS} = 10 \text{ ns}$ , respectively, and one shallow hole trap characterized by trapping and detrapping times of  $\tau_{hTS} = 4 \mu\text{s}$  and  $\tau_{hDS} = 1.2 \mu\text{s}$ . From Monte Carlo simulations, we obtain electron- and hole-transport parameters, such as electron- and hole-drift mobility,  $\mu_e = 830 \text{ cm}^2/\text{Vs}$  and  $\mu_h = 40 \text{ cm}^2/\text{Vs}$ , respectively; electron and hole surface-recombination velocities,  $s_e = 3.3 \times 10^6 \text{ cm/s}$  and  $s_h = 9.8 \times 10^4 \text{ cm/s}$ , respectively; and lifetimes of electrons and holes under pulsed bias,  $\tau_e = 2.3 \mu\text{s}$  and  $\tau_h = 3.6 \mu\text{s}$ , respectively. Significant position dependence of the lifetimes of electrons and holes inside the detector under dc bias due to hole injection is observed. We also propose a simple technique for evaluating surface recombination directly from measured current waveforms without the need for numerical simulation. Good material quality is represented by electron- and hole-mobility-lifetime products evaluated under pulsed bias of  $(\mu\tau)_e = 1.9 \times 10^{-3} \text{ cm}^2/\text{V}$  and  $(\mu\tau)_h = 1.4 \times 10^{-4} \text{ cm}^2/\text{V}$ , respectively. We identify an identical electric field profile, which is evaluated from the electron- and hole-transient currents, that validates the experimental methods used in this study.

We show that the CZTS semiconductor has good electron- and hole-transport properties, and single crystals are suitable for x-ray and gamma-ray detector fabrication.

## ACKNOWLEDGMENTS

This work is supported by the Grant Agency of the Charles University under Contract No. 1234119, by the Grant Agency of the Czech Republic under Contract No. 18-12449S, and by the U.S. Department of Energy, Office of Defense Nuclear Nonproliferation Research and Development. U.N.R. acknowledges partial support of LDRD funding from SRNL.

- [1] S. D. Sordo, L. Abbene, E. Caroli, A. M. Mancini, A. Zappettini, and P. Ubertini, Progress in the development of CdTe and CdZnTe semiconductor radiation detectors for astrophysical and medical applications, *Sensors (Basel)* **9**, 3491 (2009).
- [2] A. E. Bolotnikov, G. S. Camarda, E. Chen, R. Gul, V. Dedic, G. De Geronimo, J. Fried, A. Hossain, J. M. MacKenzie, L. Ocampo, P. Sellin, S. Taherion, E. Vernon, G. Yang, U. El-Hanany, and R. B. James, Use of the drift-time method to measure the electron lifetime in long-drift-length CdZnTe detectors, *J. Appl. Phys.* **120**, 104507 (2016).
- [3] K. Kim, A. E. Bolotnikov, G. S. Camarda, A. Hossain, and R. B. James, Overcoming Zn segregation in CdZnTe with the temperature gradient annealing, *J. Cryst. Growth* **442**, 98 (2016).
- [4] A. E. Bolotnikov, et al., Correlations between crystal defects and performance of CdZnTe detectors, *IEEE Trans. Nucl. Sci.* **58**, 1972 (2011).
- [5] T. E. Schlesinger, J. E. Toney, H. Yoon, E. Y. Lee, B. A. Brunett, L. Franks, and R. B. James, Cadmium zinc telluride and its use as a nuclear radiation detector material, *Mater. Sci. Eng. R Rep.* **32**, 103 (2001).
- [6] P. Rudolph, Non-Stoichiometry related defects at the melt growth of semiconductor compound crystals – a review, *Cryst. Res. Technol.* **38**, 542 (2003).
- [7] A. Raulo, G. Hennard, M. Sowinska, R. B. James, A. Fauler, J. Freier, A. Held, and M. Fiederle, Effects of annealing on bulk properties of CdTe detectors, *IEEE Trans. Nucl. Sci.* **60**, 3815 (2013).
- [8] M. Rejhon, J. Franc, V. Dědič, J. Pekárek, U. N. Roy, R. Grill, and R. B. James, Influence of deep levels on the electrical transport properties of CdZnTeSe detectors, *J. Appl. Phys.* **124**, 235702 (2018).
- [9] R. Gul, U. N. Roy, G. S. Camarda, A. Hossain, G. Yang, P. Vanier, V. Lordi, J. Varley, and R. B. James, A comparison of point defects in  $\text{Cd}_{1-x}\text{Zn}_x\text{Te}_{1-y}\text{Se}_y$  crystals grown by bridgeman and traveling heater methods, *J. Appl. Phys.* **121**, 125705 (2017).
- [10] U. N. Roy, A. E. Bolotnikov, G. S. Camarda, Y. Cui, A. Hossain, K. Lee, W. Lee, R. Tappero, G. Yang, R. Gul, and R. B. James, High compositional homogeneity of  $\text{CdTe}_x\text{Se}_{1-x}$  crystals grown by the bridgman method, *APL Mater.* **3**, 026102 (2015).
- [11] U. N. Roy, G. S. Camarda, Y. Cui, and R. B. James, High-Resolution virtual frisch grid gamma-Ray detectors based on as-grown CdZnTeSe with reduced defects, *Appl. Phys. Lett.* **114**, 232107 (2019).
- [12] P. Praus, E. Belas, J. Bok, R. Grill, and J. Pekarek, Laser induced transient current pulse shape formation in (CdZn)Te detectors, *IEEE Trans. Nucl. Sci.* **63**, 246 (2016).
- [13] M. Rejhon, V. Dedic, L. Beran, U. N. Roy, J. Franc, and R. B. James, Investigation of deep levels in CdZnTeSe crystal and their effect on the internal electric field of CdZnTeSe gamma-Ray detector, *IEEE Trans. Nucl. Sci.* **66**, 1952 (2019).
- [14] G. Benassi, L. Nasi, M. Bettelli, N. Zambelli, D. Calestani, and A. Zappettini, Strong mechanical adhesion of gold electroless contacts on CdZnTe deposited by alcoholic solutions, *J. Instrum.* **12**, P02018 (2017).
- [15] A. Musa, J. P. Ponpon, J. J. Grob, M. Hage-Ali, R. Stuck, and P. Siffert, Properties of electroless gold contacts on p-type cadmium telluride, *J. Appl. Phys.* **54**, 3260 (1983).
- [16] U. N. Roy, G. S. Camarda, Y. Cui, R. Gul, G. Yang, J. Zazvorka, V. Dedic, J. Franc, and R. B. James, Evaluation of CdZnTeSe as a high-quality gamma-Ray spectroscopic material with better compositional homogeneity and reduced defects, *Sci. Rep.* **9**, 7303 (2019).
- [17] S. U. Egarievwe, U. N. Roy, E. O. Agbalagba, B. A. Harrison, C. A. Goree, E. K. Savage, and R. B. James, Optimizing CdZnTeSe frisch-grid nuclear detector for gamma-Ray spectroscopy, *IEEE Access* **8**, 137530 (2020).
- [18] E. Belas, R. Grill, J. Pipek, P. Praus, J. Bok, A. Musiienko, P. Moravec, O. Tolbanov, A. Tyazhev, and A. Zarubin, Space charge formation in chromium compensated GaAs radiation detectors, *J. Phys. D Appl. Phys.* **53**, 475102 (2020).
- [19] K. Suzuki, T. Sawada, and K. Imai, Effect of DC bias field on the time-of-flight current waveforms of CdTe and CdZnTe detectors, *IEEE Trans. Nucl. Sci.* **58**, 1958 (2011).
- [20] P. Horodský, R. Grill, and P. Hlídek, Band-Edge photoluminescence in CdTe, *Phys. Status Solidi B Basic Res.* **243**, 2882 (2006).
- [21] S. Ramo, Currents induced by electron motion, *Proc. IRE* **27**, 584 (1939).
- [22] A. Musiienko, R. Grill, J. Pekárek, E. Belas, P. Praus, J. Pipek, V. Dědič, and H. Elhadidy, Characterization of polarizing semiconductor radiation detectors by laser-induced transient currents, *Appl. Phys. Lett.* **111**, 082103 (2017).
- [23] Š. Uxa, E. Belas, R. Grill, P. Praus, and R. B. James, Determination of electric-field profile in CdTe and CdZnTe detectors using transient-current technique, *IEEE Trans. Nucl. Sci.* **59**, 2402 (2012).
- [24] K. Ridzonova, E. Belas, R. Grill, J. Pekarek, and P. Praus, Space-Charge-Limited Photocurrents and Transient Currents in (Cd, Zn)Te Radiation Detectors, *Phys. Rev. Appl.* **13**, 064054 (2020).
- [25] R. Grill, E. Belas, J. Franc, M. Bugar, Š. Uxa, P. Moravec, and P. Hoschl, Polarization study of defect structure of CdTe radiation detectors, *IEEE Trans. Nucl. Sci.* **58**, 3172 (2011).
- [26] W. Shockley and W. T. Read, Statistics of the recombinations of holes and electrons, *Phys. Rev.* **87**, 835 (1952).
- [27] R. Matz and M. Weidner, Charge collection efficiency and space charge formation in CdTe gamma and X-Ray detectors, *Nucl. Instrum. Methods Phys. Res. A* **406**, 287 (1998).